

Journal of
Applied Remote Sensing



RemoteSensing.SPIEDigitalLibrary.org

Impacts of land cover change and water management practices on the Tarim and Konqi river systems, Xinjiang, China

Jonathan W. Chipman
Xun Shi
Francis J. Magilligan
Yaning Chen
Baofu Li

Jonathan W. Chipman, Xun Shi, Francis J. Magilligan, Yaning Chen, Baofu Li, "Impacts of land cover change and water management practices on the Tarim and Konqi river systems, Xinjiang, China," *J. Appl. Remote Sens.* **10**(4), 046020 (2016), doi: 10.1117/1.JRS.10.046020.

SPIE.

Impacts of land cover change and water management practices on the Tarim and Konqi river systems, Xinjiang, China

Jonathan W. Chipman,^{a,*} Xun Shi,^a Francis J. Magilligan,^a
Yanping Chen,^b and Baofu Li^c

^aDartmouth College Department of Geography, 6017 Fairchild, Hanover, New Hampshire 03755, United States

^bChinese Academy of Sciences, Xinjiang Institute of Ecology and Geography, State Key Laboratory of Desert and Oasis Ecology, 818 S Beijing Road, Urumqi, Xinjiang 830011, China

^cQufu Normal University College of Geography and Tourism, 80 Yantai Road, Rizhao, Shandong 276826, China

Abstract. The Tarim and Konqi Rivers in western China have experienced dramatic changes in streamflow and riparian vegetation due to climatic variability, land cover change, and water management including interbasin water transfers. To assess the extent and evolution of vegetation dynamics along these rivers, we use Landsat and MODIS images for land cover classification, spectral mixture analysis, and landscape phenology analysis. From 1998 to 2011, agriculture nearly tripled in extent, from 1376 to 3742 km². Natural riparian vegetation persisted in aggregate but experienced losses (to agriculture) in some areas while expanding into barren land elsewhere. Spectral mixture analysis suggests that interbasin water transfers from the Konqi to the Tarim River increased near-channel riparian vegetation on the Tarim at the expense of vegetation on the Konqi. A time-series of MODIS images reveals a pattern of increasing and decreasing greenness across the region, including loss of vegetation in distal regions that were formerly subject to sporadic seasonal flooding but now are cut off from their water supply due to water management. These results suggest that satellite remote sensing may play a valuable role in monitoring the effects of changing land use and hydrology on riparian systems in Central Asia and other arid regions. © 2016 Society of Photo-Optical Instrumentation Engineers (SPIE) [DOI: [10.1117/1.JRS.10.046020](https://doi.org/10.1117/1.JRS.10.046020)]

Keywords: Xinjiang; Tarim; land cover; spectral mixture analysis; interbasin water transfers.

Paper 16516 received Jul. 8, 2016; accepted for publication Nov. 11, 2016; published online Dec. 1, 2016.

1 Introduction

China's arid western Xinjiang Uyghur Autonomous Region is experiencing rapid population growth, economic development, and pressures from interannual- to decadal-scale climate variability superimposed on long-term anthropogenic climate change. All of these factors affect water management and water security in multiple ways. At the same time, water management decisions and concerns over water security contribute to an environment of conflict and competition among stakeholders divided along ethnic, religious, economic, and administrative lines.

These processes are particularly evident in Southern Xinjiang, including the Tarim Basin.¹ The Tarim is China's longest internal river and is primarily sourced from precipitation in the surrounding mountain ranges, including the Tian Shan, Pamir, and Kunlun, including past precipitation stored in montane glaciers. Beginning in the 1960s, the construction of dams and the withdrawal of water from the river for agriculture, industry, and domestic consumption led to a dramatic reduction in flow in the lower reaches of the river, as well as the disappearance of

*Address all correspondence to: Jonathan W. Chipman, E-mail: jonathan.w.chipman@dartmouth.edu

its terminal lake, Taitema. More recently in 2000, the government commenced an intermittent series of within-basin and interbasin water transfers, with the ostensible objective of restoring degraded riparian systems along the lower river.² These transfers involved releases of water from upstream reservoirs on the Tarim, as well as diversion of water from the Konqi River into the Tarim River.

Researchers in the region have documented some of the effects of these changes over the past decades, including the impacts of climate change and interannual variability on glaciers^{3,4} and streamflow,^{1,5} the response of riparian ecosystems and groundwater to changes in streamflow,^{2,6–8} and the connections between population growth, economic development, land use, and water management.⁹

Given the broad spatial scale of the Tarim and Konqi river systems, remote sensing provides a valuable tool for more spatially expansive assessments of the nature and impacts of these changes in land cover and water management, including their effects on downstream ecosystems both proximal and distal to the rivers' channels. Previous research in this region¹⁰ used moderate-resolution (Landsat and SPOT) imagery to study land cover change trajectories for one township in the Yuli oasis. Coarser-resolution imagery from SPOT-vegetation and Terra/Aqua MODIS has also been employed^{11,12} to assess vegetation dynamics at broader scales within the Tarim Basin.

In this study, we expand on that prior research, using multiple complementary remote sensing data sources and analytical methods synergistically to examine the ways the middle and lower reaches of the Tarim River, the neighboring and interconnected Konqi River, and their surrounding landscapes have responded over the past decade to changing environmental conditions, land use, and water management policies. The use of several distinct data sources and analytical methods (land cover classification, spectral mixture analysis, and landscape phenology analysis) should provide a more robust, nuanced, and reliable assessment than any one sensor and methodology alone. Using these data, we seek to understand how ecosystem responses have differed along multiple dimensions (upstream versus downstream, Tarim versus Konqi, and proximal versus distal zones). Ultimately, we hope to provide guidance for local resource managers and other stakeholders on the use of satellite remote sensing for assessing the rapid changes in land use and vegetation cover across this region, and for evaluating the impacts of water management policies, such as within-basin and interbasin water transfers.

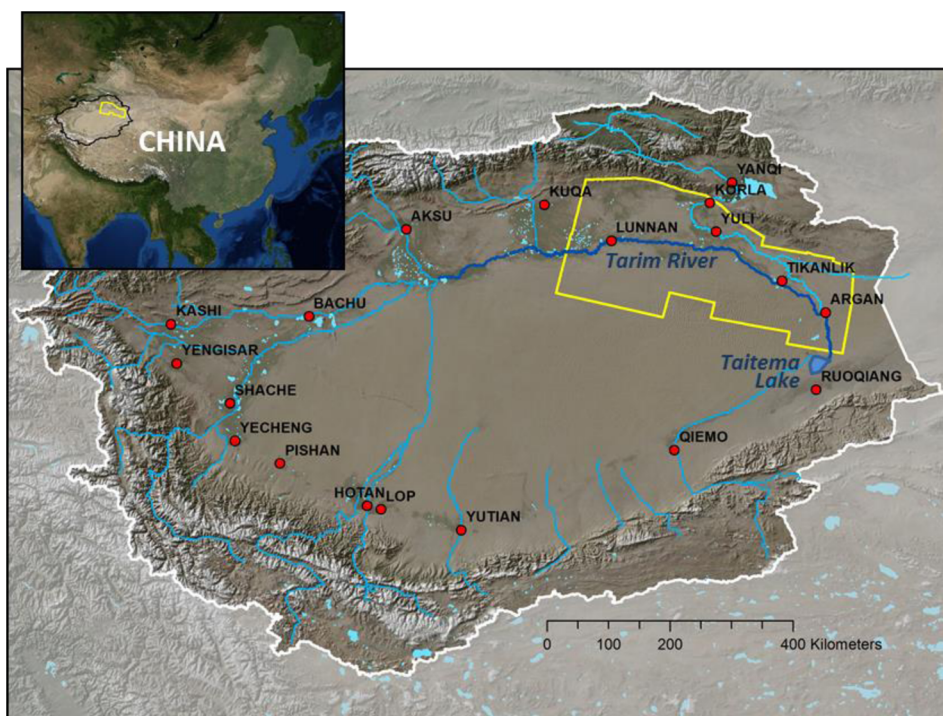


Fig. 1 Map of the study area (yellow polygon) within the Tarim/Konqi Basin in western China.

1.1 Study Region

The study region (~79,000 km² area) covers the lower reaches of the Tarim River, the neighboring Konqi River, and their surrounding landscapes. These river systems are located at the northern fringe of the Taklimakan Desert and the south slope of the Tian Shan range (elevations exceeding 5000 m), largely defined by 83.2°E to 88.9°E and 39.5°N to 42.1°N (Fig. 1). As noted, the construction of large dams and reservoirs from the 1960s onward led to decreased flow in downstream sections of the Tarim River, such that the last 320 km of the river had been completely dry for 30 years before the first water conveyances.² Consequences of this drying included a lowering of the water table, the loss of riparian vegetation, and concerns about the windborne mobilization of previously stabilized desert soils. During this same period, the region also experienced increased but highly variable warming, leading to large interannual fluctuations in river discharge, complicating the water management process.^{13–15} Climate models replicate this effect in hindcasting and project that it will likely continue over the 21st century.¹⁶ Within the Tian Shan range, spatially varying trends in precipitation, snow cover, glacier mass balance, and streamflow have been observed.^{3,5,17} Overall, in the past 20 years, the area witnessed increasing runoff, likely due to both locally increased precipitation and progressive melting of mountain glaciers in response to increasing temperature.

1.2 Water Conveyances in the Early 21st Century

Water management in the Tarim-Konqi region, as in most of Xinjiang, is intensive. In recent years, a series of major water system engineering projects have been built in the region, with additional future construction proposed. These artificial manipulations of the riparian environment include dams for water storage and hydropower, canals and other irrigation-related structures, roadways, industrial facilities, and hard engineering efforts such as channelization. In the late 20th century, the government adopted a plan “ecological water conveyance on the Tarim River” to ameliorate the acute water shortages of the Tarim River. Water was transferred to the lower Tarim via releases from reservoirs on higher reaches of the Tarim River itself as well as from the neighboring Konqi River. From 2000 to 2011, 12 “water conveyances” occurred (Table 1), in most cases releasing enough water to reach all the way to the river’s end at Taitema Lake.

Table 1 Twelve water conveyances on the Tarim River, Xinjiang, China.

Conveyance	Start month	End month	Transported water (million m ³)	Distance reached in the Tarim River (km)
1	May 2000	June 2000	98	106
2	October 2000	February 2001	226	218
3	April 2001	November 2001	382	360 (reached Taitema Lake)
4	June 2002	November 2002	331	360 (reached Taitema Lake)
5	March 2003	November 2003	623	360 (reached Taitema Lake)
6	April 2004	June 2004	102	360 (reached Taitema Lake)
7	May 2005	October 2005	282	360 (reached Taitema Lake)
8	June 2006	November 2006	201	360 (reached Taitema Lake)
9	September 2007	October 2007	14	105
10	November 09	December 2009	11	115
11	June 2010	November 2010	390	360 (reached Taitema Lake)
12	January 2011	January 2011	36	360 (reached Taitema Lake)

The conveyances were carried out ostensibly to restore degraded riparian ecosystems along the lower Tarim. While there have been several studies of the effects of these transfers on the lower Tarim,^{2,18} minimal attention has been paid to the broader impacts beyond the immediate riparian zone of the lower reaches of the Tarim River. This has left unaddressed the question of whether these water conveyances are merely transferring the environmental and social benefits of water availability from less-visible areas to more-visible areas.

2 Methods

As noted in Sec. 1, several previous studies have used remote sensing methods to examine land cover change in portions of the Tarim Basin. Until now, however, no broad-scale study in this region has made use of the synergy between multiple sensors (Landsat and MODIS), analytical approaches (spectral mixture analysis, rule-based classification, and landscape phenological analysis), and comparisons across landscape units (upstream versus downstream, Tarim versus Konqi Rivers, and proximal riparian zones versus distal areas). To best accomplish this, three different approaches were used to analyze landscape change in the study region

- a. Spectral classification of Landsat-5 and -7 images into land-use/land-cover categories.
- b. Spectral mixture analysis of the same Landsat images, to determine the actual percent cover of vegetation on a per-pixel basis.
- c. Analysis of seasonal variability and long-term trends in 250-m spatial resolution MODIS normalized difference vegetation index (NDVI) data.

Each of these approaches yielded information about the spatial extent and temporal changes in agricultural lands and natural (unmanaged) plant communities. By comparing the results from these three complementary analytical approaches, we sought to obtain a more complete, robust, and convincing picture of land use/land cover change than could be provided by any one of the methods on its own, and to shed light on the ecological impacts of the interbasin water transfers, climate variability, and other factors driving riparian change in this region.

2.1 Landsat Image Preparation

Table 2 lists the Landsat images used for analyses (a) and (b). Because of the wide extent of the study area, six images were required for each year. Five years (1998, 2000, 2007, 2009, and 2011) offered high-quality, cloud-free images during the summer season, although one portion of the area had no cloud-free imagery in 1998 so an earlier image was used (Table 2). A majority (77%) of the images were acquired in August and September, with the remainder as close to this 2-month window as possible. For comparison, based on MODIS vegetation index data (Sec. 2.4), the greenness of cotton fields in this region rises above background levels in early April, reaches a peak in early July, and subsides back down to background levels in late November. Unmanaged riparian vegetation has a weaker seasonal cycle in this area, but it likewise has a peak in early July followed by a long, slow decline in greenness into late

Table 2 Landsat images in this study. Dates are in YYYY-MM-DD format for each path/row (P/R) combination. No suitable cloud-free image was available for P142 R032 during summer 1998, so a 1990 image was substituted.

Year	P141/R032	P142/R032	P143/R031	P143/R032	P144/R031	P144/R032
1998	1998-09-06	1990-10-09	1998-09-04	1998-09-04	1998-09-27	1998-09-27
2000	2000-10-13	2000-09-18	2000-09-17	2000-09-17	2000-08-07	2000-08-07
2007	2007-08-30	2007-07-20	2007-09-13	2007-09-13	2007-05-31	2007-08-19
2009	2009-09-20	2009-08-10	2009-08-01	2009-08-01	2009-09-09	2009-08-08
2011	2011-08-25	2011-07-31	2011-08-07	2011-08-07	2011-07-13	2011-07-13

November or December. All 30 Landsat images were obtained from the US Geological Survey (USGS).¹⁹

The images were provided by USGS with pixel values as scaled integers [digital numbers (DNs)] proportional to the top-of-atmosphere spectral radiance (L_λ , in $\text{Wm}^{-2} \text{sr}^{-1} \mu\text{m}^{-1}$). For each path/row combination, all five dates of imagery were visually screened for clouds, dust, aerosols, and other atmospheric phenomena, and then a common area of overlap was delineated and extracted, within which all five images provided high-quality data.

Even after this visual screening process, spatial and temporal variation in atmospheric scattering and absorption would be expected to cause variations in the top-of-atmosphere upwelling spectral radiance among these 30 images. This would happen even when no actual change occurs on the surface, although given the relatively dry atmosphere in this arid region such atmospheric effects might be expected to be less significant than in a more humid area. Because all ground truth data for the study were obtained at the end of the time series (2012), it was essential to minimize this interimage variability in top-of-atmosphere spectral radiance associated with changing atmospheric conditions.

Two methods for reducing extraneous interimage variance in the spectral data were considered. Initially, a widely used atmospheric correction method²⁰ was employed to model at-surface spectral reflectance (ρ_λ). However, comparison of the resulting spectral reflectance values for temporally stable targets (e.g., unvegetated rock outcrops and sand dunes) showed that substantial differences in ρ_λ persisted despite the correction process, perhaps due to incomplete modeling of atmospheric conditions.

Had *in situ* observations of downwelling spectral irradiance been available for all 30 Landsat image locations and dates, it might have been possible to perform a more rigorously deterministic atmospheric correction process to produce temporally stable estimates of at-surface spectral reflectance. In the absence of such data, an empirical image normalization process was used instead, as defined in Eq. (1) below and implemented using the spatial modeler in ERDAS Imagine. This normalization process was based on identifying a set of temporally stable targets (as defined in the preceding paragraph) whose inherent spectral reflectance patterns should not change from image to image. The scaled spectral radiance measurements (DNs) for each image were adjusted so that their mean values were consistent at these temporally stable targets. First, the five temporal images for each path/row combination were radiometrically normalized to match their mean values at the stable targets

$$L_{\lambda,i,p,\text{post}} = (L_{\lambda,i,p,\text{pre}} - L_{\lambda,i,t,\text{pre}}) \left(\frac{\bar{\sigma}_{\lambda,t}}{\sigma_{\lambda,i,t,\text{pre}}} \right) + \bar{L}_{\lambda,t}, \quad (1)$$

where $L_{\lambda,i,p,\text{post}}$ is the postnormalization value for pixel p at wavelength λ in image i , $L_{\lambda,i,p,\text{pre}}$ is the prenormalization value for pixel p at wavelength λ in image i , $L_{\lambda,i,t,\text{pre}}$ is the prenormalization value for stable target t at wavelength λ in image i , $\bar{\sigma}_{\lambda,t}$ is the mean of standard deviations of values for stable target t at wavelength λ over all image dates, $\sigma_{\lambda,i,t,\text{pre}}$ is the prenormalization value for stable target t at wavelength λ in image i , and $\bar{L}_{\lambda,t}$ is the mean value of stable target t at wavelength λ over all image dates.

Next, stable targets within the area of overlap between adjacent path/row combinations were used in a similar fashion for radiometric normalization across paths and rows. In principle, this temporal and spatial normalization process should result in all 30 images having a nearly uniform spectral “signature” for a given surface feature type.

To further reduce extraneous image-to-image variability in L_λ , Landsat spectral bands 1 (0.45 to 0.52 μm wavelength) and 2 (0.52 to 0.60 μm) were discarded. These short-wavelength bands are the most strongly affected by Rayleigh scatter in the atmosphere, whereas the at-surface spectral reflectance in these bands is generally very highly correlated with that of the longer-wavelength band 3 (0.63 to 0.69 μm) that is less affected by scatter. Thus, by omitting these two bands, the effect of Rayleigh scatter can be greatly reduced without a large loss in information content.

The six images providing spatial coverage for each year were then mosaicked in preparation for classification and spectral mixture analysis. With null values being encoded as zero in the input images, the mosaicking process (in ArcGIS) took the highest value for each pixel in areas of overlap, so that null values would never replace valid data in the mosaic.

2.2 Landsat Image Classification

A rule-based classification procedure was used to classify each annual image mosaic into five generalized information classes: water, agricultural crops, natural (nonagricultural) vegetation, and two different classes of unvegetated desert (one primarily sand dunes and other aeolian features, the other interbedded sand and silt layers in previously inundated areas). Urban areas, roads, and other similar features were omitted from the classification scheme due to their sparse extent within the study region. Field observations from August 2012 were used to help interpret spectral patterns in the 2011 imagery, and these spectral patterns were then used to classify all image dates, since the normalization process described previously should ensure that the same surface feature types in each image have similar spectral “signatures.” Note that this procedure assumes that features seen on the ground in 2012 were unchanged from 2011, but does not require them to have been unchanged in the previous years.

The radiometric normalization and image classification processes are shown in Fig. 2. The classification was implemented using the ERDAS imagine spatial modeler, with the same model used to classify all 5 years of imagery. The image parameters used in the rules were as follows:

- Scaled spectral radiance (DN) in the red and near-infrared bands (bands 3 and 4 on Landsat-5 and -7).
- Normalized difference ratio based on near-infrared and red bands (NDVI).
- Normalized difference ratio based on mid-infrared and red bands [ND53; (band 5 – band 3)/(band 5 + band 3)].

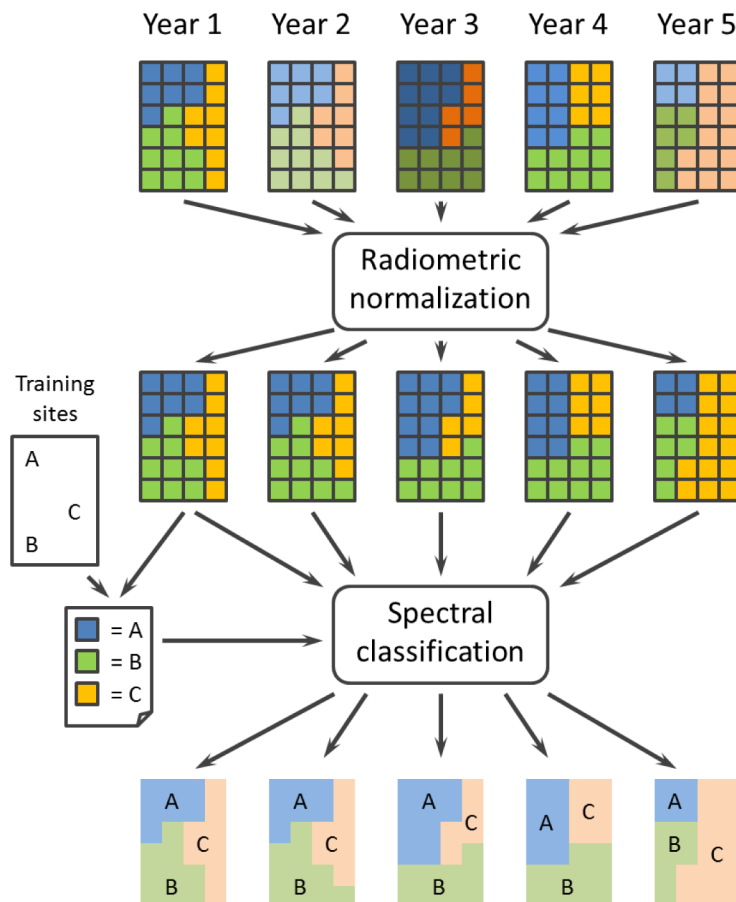


Fig. 2 Radiometric normalization and classification of Landsat images. Row 1: five dates of imagery for the same area, showing spectral variations due to atmospheric conditions and land cover change. Row 2: normalized images showing land cover change only, after compensation for atmospheric conditions. Row 3: classified output for each date, using rules based on spectral patterns and information from field-visited training sites.

Table 3 Rules for classification of the Landsat images. B3 and B4 are radiometrically normalized Landsat TM or ETM+ scaled spectral radiance (DN) in bands 3 and 4.

Order	Rule	Outcome if true
1	(B3 = 0)	Unclassified
2	(B3 > 0) and (NDVI < -0.09) and (B4 < 40)	Class 1 (water)
3	(B3 > 0) and (NDVI > 0.24)	Class 2 (agriculture)
4	(B3 > 0) and (NDVI = 0.0 to 0.24)	Class 3 (natural vegetation)
5	(B3 > 0) and (ND53 > 0.15) and (NDVI = -0.09 to 0.0)	Class 4 (sandy soil)
6	(B3 > 0) and (ND53 <= 0.15) and (NDVI = -0.09 to 0.0)	Class 5 (sand/silt)

The specific rules used in the model are listed in Table 3.

Many different methods have been described for accuracy assessment of remotely sensed image classification.²¹ In general, different sampling schemes provide different advantages and disadvantages. For this project, an ideal accuracy assessment scheme would include the following:

1. Randomness (to ensure that samples are representative of the area);
2. Stratification (to ensure adequate sampling of sparsely distributed classes);
3. Adequate sample size (to provide a robust estimate of accuracy); and
4. Accessibility of sites in the field (for *in situ* verification).

Unfortunately, there are strong conflicts among some of these preferred values (e.g., given the remoteness of the study region and the physical and administrative limitations on travel, a completely randomized design would be impractical in terms of accessibility). To circumvent this problem, two separate accuracy assessments were conducted, one based on a stratified random sample of 250 points that were photointerpreted from high-resolution imagery but not visited in the field, and a separate assessment based on 169 points that were visited in the field but with no randomization (the field-visited points were selected on an *ad hoc* basis biased toward proximity to roads).

For the stratified random sample, 50 points were generated at completely randomized locations within the set of pixels classified as each land cover class in the 2011 image, and their “true” class interpreted by examination of high-resolution satellite imagery (primarily true-color images from the WorldView-2, GeoEye-1, or QuickBird satellites; all of which are an order of magnitude higher spatial resolution than Landsat) provided via the ESRI imagery web map service.²² This photointerpretation was performed by an analyst who was uninvolved in the Landsat classification and who did not have access to the classification results. At the scale of the high-resolution imagery, the interpreter was able to see individual shrubs and other small features with sufficient detail to differentiate among the relatively broad set of land cover classes used here.

For both of the accuracy assessments, an error matrix was produced, from which the overall accuracy and class-specific user’s and producer’s accuracy estimates were derived. In addition, for the photointerpreted sample, the $\hat{\kappa}$ coefficient and its variance were calculated. $\hat{\kappa}$ provides an adjusted estimate of classification accuracy that compensates for the expected fraction of correctly classified samples due to random chance. While there is disagreement²³ within the field concerning the utility and validity of $\hat{\kappa}$, it continues to be widely reported (and often expected) in assessments of classification accuracy. The method for calculating the variance of $\hat{\kappa}$ was chosen for suitability with a stratified random sample.²⁴ Since calculating $\hat{\kappa}$ and its variance for an *ad hoc* (nonrandom) sampling scheme is problematic, these estimates were only reported for the photointerpreted sample, not the field-visited sample.

2.3 Landsat Image Spectral Mixture Analysis

The “hard” categories produced by the rule-based classification process can provide one way of quantifying land cover change, e.g., denoting the number of hectares that transitioned from

classes A to B during the interval between two images. However, more subtle landscape changes may not be drastic enough to register as a full transition between classes. For example, increased water availability might lead to a gradual increase in the percent cover of vegetation within a given image pixel. To assess these kinds of subpixel changes in vegetation cover, we used linear spectral unmixing, implemented using spectral mixture analysis algorithms in ENVI 5.0, with the same set of 30 Landsat images from Sec. 2.2.

The linear spectral unmixing process assumes that the spectral pattern associated with a given pixel in an image can be modeled as a linear mixture of two or more “pure” spectra, each weighted by its fractional area of coverage within the pixel.²⁵ These pure spectra, or endmembers of the linear mixture model, were extracted from areas of the imagery that were expected to have as close to 100% cover as possible from a single land cover class (water, vegetation, and patches of two unvegetated soil classes in the desert—sand dunes and flat-lying, light-toned silty soil).

The output from the mixture model consists of one raster layer for each land cover type, with each pixel containing the percent cover of that land cover type within the given pixel. A pixel that includes part of a river, plus a sandy area with scattered shrubs, might be inferred to have 0.35 (35%) coverage of water, 0.50 (50%) coverage of sand, and 0.15 (15%) of vegetation. If, over time, groundwater levels in that pixel increased due to infiltration from the river channel, the vegetation fraction might increase while the sand fraction correspondingly decreases.

One common anomaly in this process is the presence of pixels with fractional cover that exceeds the [0...1] range for a given class. Since fractional cover <0 or >1 is physically unrealistic, this is considered an artifact of errors in the selection of endmembers or the assumptions in the mixture model. Often the cause is the presence of one or more pixels whose spectra are more “extreme” than the pixels chosen as “pure” endmembers for the model—if the training area used to extract the vegetation pure spectrum only has 95% cover of vegetation, but is assumed to be 100%, then any pixel whose actual percent cover exceeds 95% may produce a fractional cover >1.0 in the output. There are a variety of ways of handling this problem; for this study, fractional cover was truncated at 0 and 1.

2.4 Analysis of Landscape Phenology and Decadal Trends with MODIS Imagery

The Landsat imagery used for classification and linear spectral unmixing provides relatively high-spatial resolution at coarsely spaced and irregular temporal intervals (1998, 2000, 2007, 2009, and 2011). To complement this, we used imagery from the Terra and Aqua MODIS instrument at a coarser spatial scale (250 m pixels) but very fine temporal resolution (one image every 8 to 16 days, from February 2000 to the present).

The MODIS images were obtained from the MODIS data pool at the land processes distributed active archive facility (LP-DAAC), as MOD13Q1 vegetation index data. Each of the 544 images includes two vegetation indices, the NDVI, and enhanced vegetation index, plus additional ancillary data. Each image represents a composite of the best cloud-free data obtained by one satellite (Terra or Aqua) during a 16-day window. Following the launch of Aqua in mid-2002, the 16-day composites from the two satellites are offset by half a cycle, so as to provide one image every 8 days. The vegetation index data sets were kept in their original sinusoidal coordinate system during the data processing and analysis steps, to avoid loss of information via resampling, but were reprojected to an Albers equal-area coordinate system for visual display in Figs. 3 and 8.

Figures 3 and 4 show the nature of this time series of 544 vegetation index images. In Fig. 3, a single composite NDVI image (for the 16-day period starting on 2 June 2011) is shown in grayscale, with brighter pixels representing higher vegetation index values, and thus a higher fractional coverage of photosynthetically active vegetation. Figure 4 shows the full time series of NDVI values for two individual pixels extracted from the “stack” of images. One pixel is located on a farm that was under cultivation for the entire period, and thus shows a strong seasonal cycle in all years. The second pixel is on a newly established farm; its NDVI time series shows an initial period of low NDVI values, followed by years with higher NDVI and stronger seasonal cycles in later years once the farm was in operation.

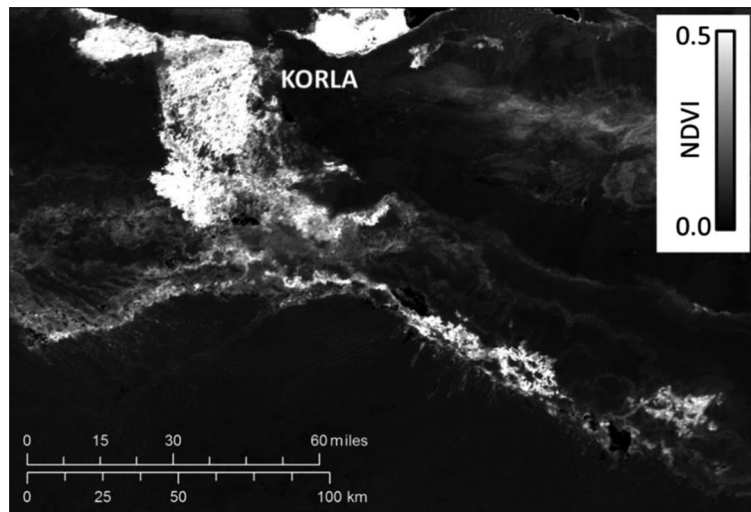


Fig. 3 MODIS NDVI vegetation index image (June 2, 2011).

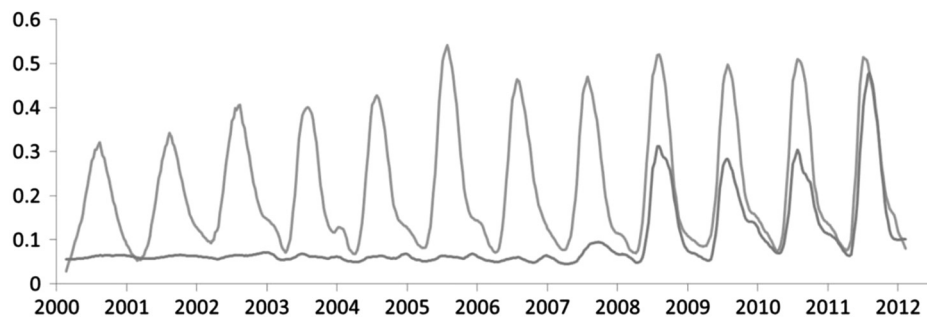


Fig. 4 MODIS NDVI time series of vegetation index data (Y-axis), for two farm fields.

“Temporal signatures” like those shown in Fig. 4 were extracted for areas of interest in the MODIS vegetation index data set. Due in part to the coarse spatial scale and the inconsistent relationship between the spatial positions and extents of ground resolution cells in the daily level-0 MODIS imagery versus the gridded 16-day MOD13Q1 composite images, there is a substantial amount of noise in the raw NDVI data. To highlight seasonal and interannual trends, an LOESS-smoothed version of the NDVI time series was also derived for all extracted temporal signatures, using a 12-point timescale.^{26,27}

Finally, decadal trends in NDVI were also calculated for all MODIS pixels in the study area, using an ordinary least squares approach, implemented using scripts we developed for the ERDAS imagine spatial modeler. This method²⁸ minimizes the sum of the squares of residuals (differences between the modeled and the observed values), based on the following equation:

$$b_{1,j} = \frac{\sum(x_i y_{ij})}{\sum x_i^2}, \quad (2)$$

where $b_{1,j}$ is the NDVI trend for pixel j (per year; multiply by 10 for decadal trend), x_i is the date of image i , expressed as decimal year (e.g., 2010.495), and y_{ij} is the NDVI value for pixel j in image i .

These temporal signatures and decadal trends were examined for various landscape units within the study region (e.g., riparian buffer zones versus areas away from rivers) to provide an alternative view of landscape change within the region, complementing the analyses of Landsat image classification and spectral mixture modeling.

3 Results

3.1 Landsat Image Classification

Figure 5 shows the results of the land cover classification process. Similar classified maps were produced for all 5 years, allowing changes in land cover to be assessed from 1998 to 2011. As shown in panels (c) and (d) of this figure, one of the most striking changes during this time period was the rapid expansion of irrigated agriculture in the major oases (the enlargements in Fig. 5 are for the Korla/Yuli oasis) and along rivers.

The spatial extent of water on the landscape fluctuated widely. Open water in rivers, lakes, and reservoirs totaled only 27 km² in 2009 but covered 496 km² in 1998. Agriculture nearly tripled in area, increasing from 1376 km² in 1998 to 3742 km² in 2011 (Table 4). Given that essentially all of this agricultural land requires irrigation, this expansion will clearly impose

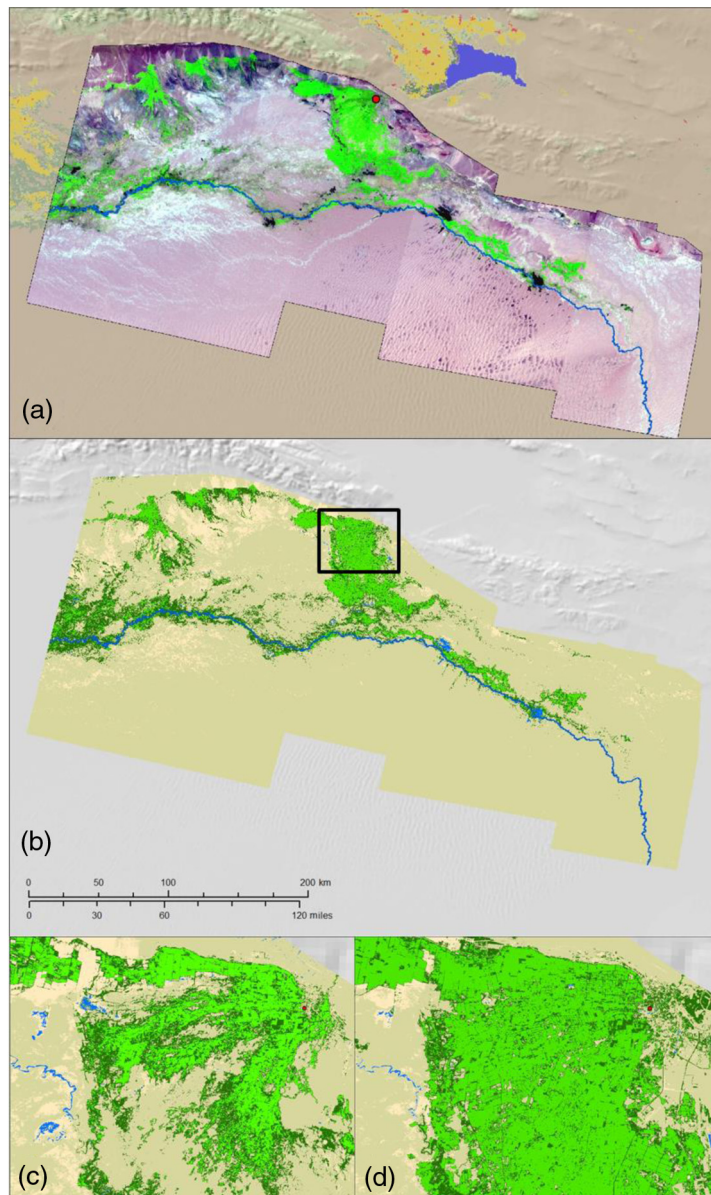


Fig. 5 Examples of Landsat image classification results. (a) Normalized Landsat mosaic (2011), bands 5, 4, 3 as RGB. (b) Classification from (a). (c) and (d) Enlargements of the Korla oasis from 1998 and 2011, respectively, showing rapid expansion of irrigated agriculture. In classified images, light green indicates agricultural land, dark green is natural vegetation, blue is water, and tan shades are two classes of unvegetated desert soils.

Table 4 Area of selected land cover classes within the study region, 1998 to 2011.

Year	Surface water (area, km ²)	Agriculture (area, km ²)	Natural vegetation (area, km ²)
1998	496	1376	5886
2000	347	1719	6056
2007	159	2845	6749
2009	27	2942	5819
2011	180	3742	5966

a corresponding demand for water on the region's water management. Meanwhile, over the course of the study period, natural (unmanaged) vegetation remained relatively stable in its net extent, from 5886 km² in 1998 to 5966 km² in 2011 (Table 4), but experienced losses in some areas and increases in others.

The results of the two accuracy assessments for the land cover classifications were provided as error matrices in Tables 5 and 6. Table 5 presents the results of the random, photointerpreted sample, whereas Table 6 shows the nonrandom but field-visited sample. In each case, the rows of the matrix show the distribution of sample points by their mapped class, whereas the columns show the distribution of points by their "true" class.

For the random sample of photointerpreted points, the overall accuracy was 91%, and $\hat{\kappa}$ was 0.89 (2 σ range 0.86 to 0.92). All of the class-specific producer's and user's accuracy values were >80% with the exception of the user's accuracy for the sand-silt class of desert soils (76%). The most frequent errors were as follows:

- *Areas of natural vegetation misclassified as sand-silt desert soils:* The majority of these were sites where scattered shrubs occur on relatively bright, high-reflectance soil. In some cases, the shrubs may be very sparse, or dormant, or have a particularly low leaf-area index. It is likely that the sensor and classifier were responding to the dominant soil reflectance signature rather than the weaker vegetation signature.
- *Agricultural fields misclassified as natural vegetation:* These are typically cases where an obvious rectangular field was constructed on the ground in preparation for cultivation, but no crop was present at the time of the Landsat image. These were either new fields or fields that were fallow. Since these fields were presumably not being irrigated at the time of

Table 5 Accuracy assessment error matrix from photointerpreted sites. Numbers on the major diagonal, in bold face, were correctly classified. Overall accuracy was 91%, $\hat{\kappa}$ was 0.89 (2 σ range 0.86 to 0.92).

		Validation data (from high-resolution photointerpretation)						
		Water	Agric.	Nat-veg	Sand	Sand-silt	Row total	User's accuracy (%)
Classification results	Water	49	0	0	0	1	50	98
	Agric.	0	50	0	0	0	50	100
	Nat-veg	0	6	44	0	0	50	88
	Sand	0	0	3	47	0	50	94
	Sand-silt	3	1	7	1	38	50	76
	Column total	52	57	54	48	39	250	
	Producer's accuracy (%)	94	88	81	98	97		

Table 6 Accuracy assessment error matrix from field-visited sites. Numbers on the major diagonal, in bold face, were correctly classified. Overall accuracy was 89%.

		Validation data (from <i>in situ</i> observation)					User's accuracy (%)	
		Water	Agric.	Nat-veg	Sand	Sand-silt	Row total	
Classification results	Water	4	0	0	0	0	4	100
	Agric.	0	23	0	0	0	23	100
	Nat-veg	0	2	47	0	0	49	96
	Sand	0	0	10	66	5	81	81
	Sand-silt	1	0	0	0	11	12	92
	Column total	5	25	57	66	16	169	
	Producer's Accuracy (%)	80	92	82	100	69		

image acquisition, this “misclassification” may actually have been preferable in terms of understanding the water management demand.

The results of the second accuracy assessment, based on field-visited rather than photointerpreted points, were shown in Table 6. Overall accuracy (89%) was quite similar to that from the randomized assessment but the class-specific user’s and producer’s accuracies varied, as can be seen by comparing Table 6 to Table 5. In terms of user’s accuracy, the field-based accuracy assessment suggested a higher level of accuracy for the natural vegetation and sand-silt classes (compared to the photointerpretation-based assessment), but a lower accuracy for sand alone.

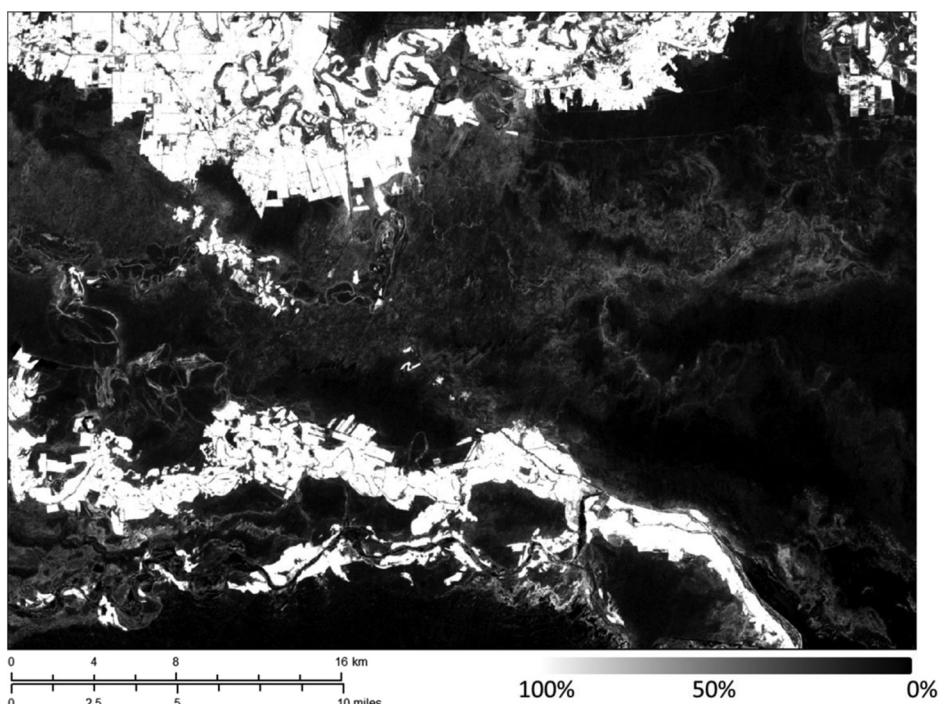


Fig. 6 Example of a vegetation fraction output layer, from linear spectral unmixing. Pixel brightness represents the percent cover of vegetation from 100% cover (white) to 0% cover (black). The area shown is at the southern edge of the Korla/Yuli oasis, with the Konqi River at top and the Tarim River at bottom.

For producer's accuracy, the field-based assessment showed a lower accuracy for water and sand-silt, but slightly higher accuracies for all other classes.

3.2 Landsat Image Spectral Mixture Analysis

The spectral mixture analysis process resulted in a series of layers representing the fractional cover of each major land cover class (water, vegetation, and soil classes) for each of the 5 years. Figure 6 shows a representative example of the output, for the vegetation fraction layer in 2011, in an area south of Yuli near the Tarim and Konqi Rivers. Bright pixels represent higher fractional coverage of vegetation, whether agricultural crops or particularly dense patches of natural riparian vegetation. Darker gray pixels are areas with sparser vegetation cover (primarily scattered shrubs in the desert) and black pixels are unvegetated areas (water or bare sand). One particularly notable aspect of Fig. 6 is the distinct patterns of sparse but still extant vegetation following the dense network of meandering former river channels between the current channels of the Tarim and Konqi Rivers. These faint gray patterns extend from left to right across the center of the image in Fig. 6 and will be discussed further below.

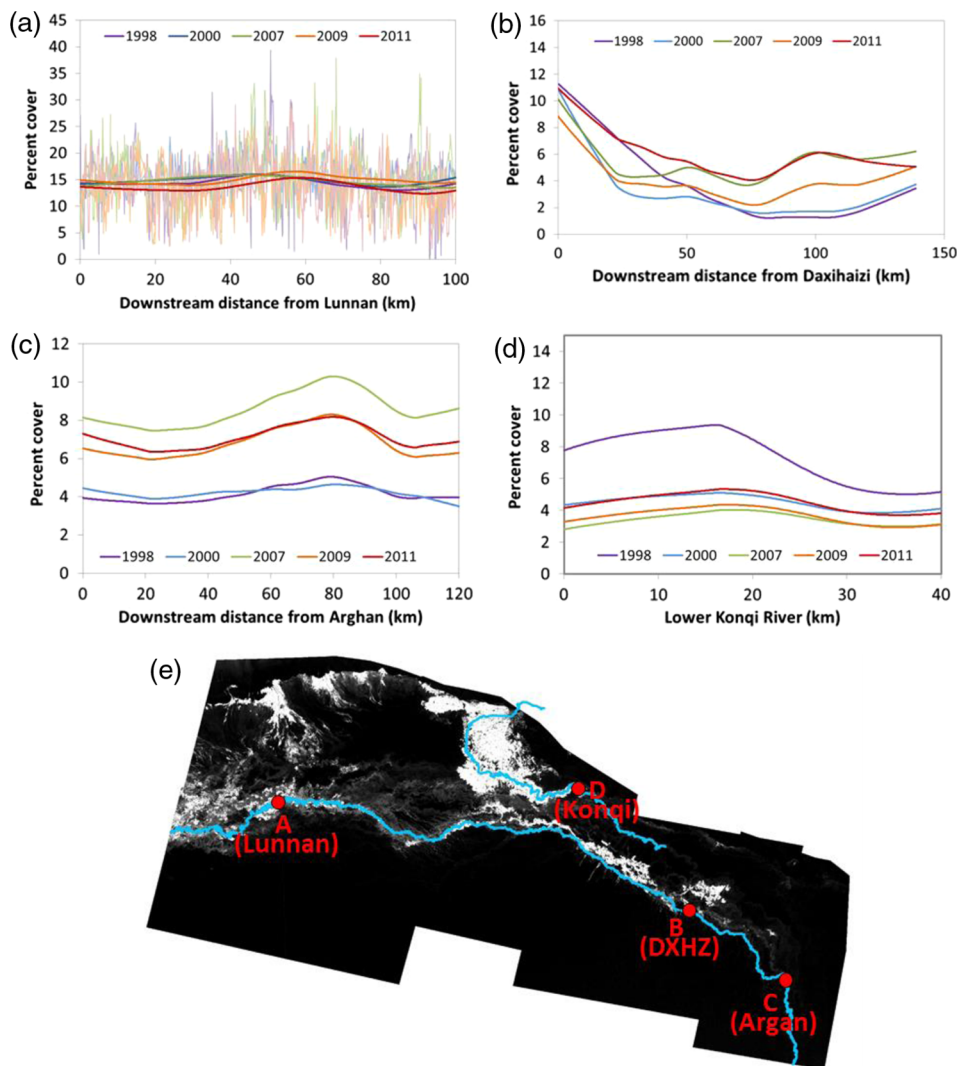


Fig. 7 Fractional cover of vegetation within 120 m riparian buffer zone, along four reaches of the Tarim and Konqi Rivers. (a) Upstream on the Tarim River near Lunnan. (b) and (c) Downstream below the dam at Daxihaizi, and below Argan. (d) Konqi River downstream from the Yuli oasis. In (a), the full data are shown in thin lines with a LOESS-smoothed version superimposed; in (b)–(d) only the LOESS versions are shown. (e) Locations of the graphs shown in (a)–(d), superimposed on the 2011 fractional vegetation cover map.

To explore the effects of the post-2000 water conveyances on the lower Tarim River, we examined the percent cover of vegetation within a 120-m riparian buffer zone, in all 5 years (1998, 2000, 2007, 2009, and 2011). Pixels classified as water or agriculture were excluded from this analysis, to focus on natural riparian vegetation communities. As shown in Fig. 7(a), at Lunnan—far upstream from the conveyances—water was relatively abundant in all years and there was no discernable change in riparian vegetation cover from year to year. Downstream, however, at Daxihaiizi (b) and Argan (c), there was a clear increase in riparian vegetation cover,

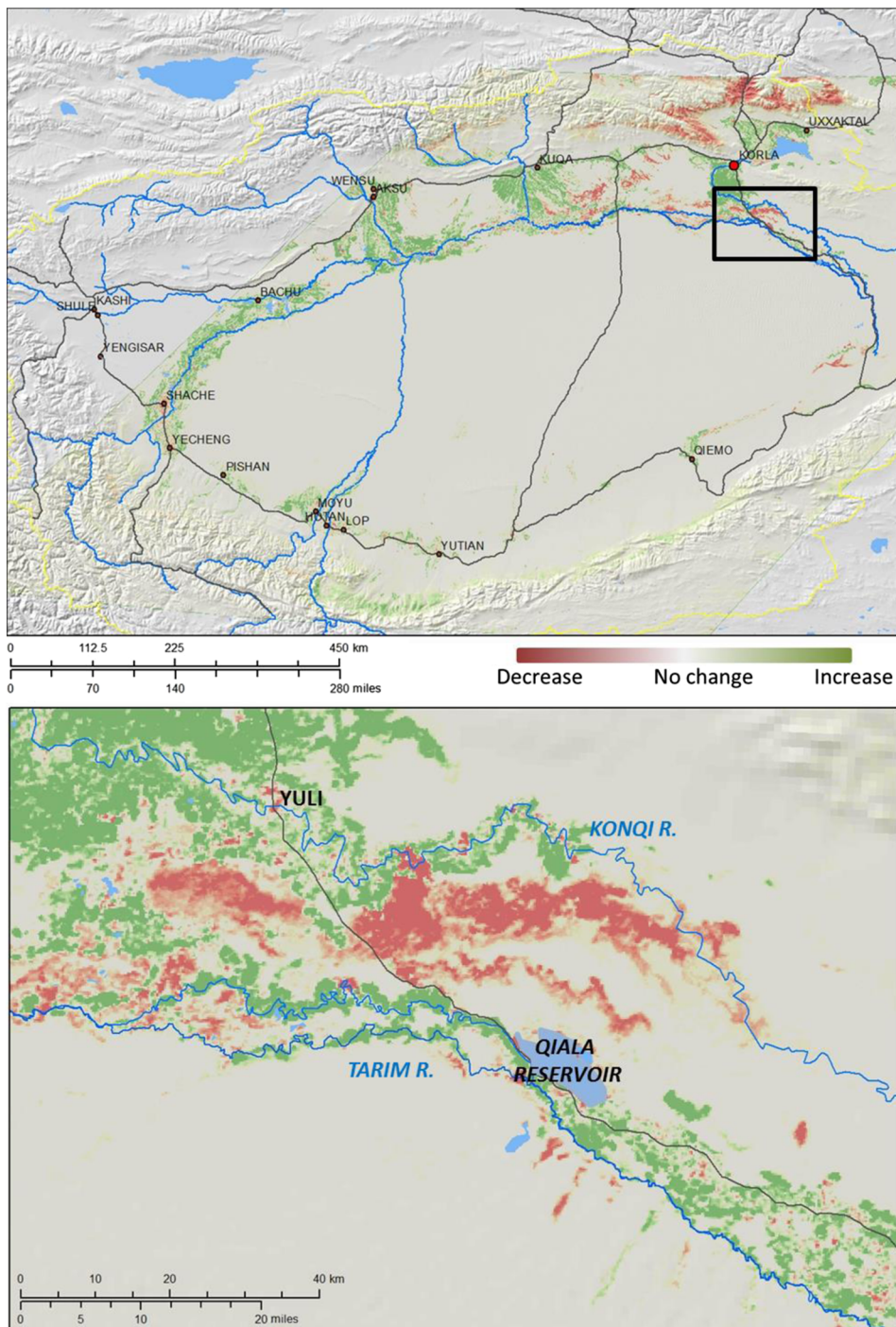


Fig. 8 Decadal trend in MODIS vegetation index series, for the entire basin (top) and for the Tarim/lower Konqi River area (bottom). Green pixels represent increasing index values, whereas brown pixels represent decreases.

with all post-2000 years being higher than 1998 or 2000. Meanwhile, on the lower Konqi River, there was an actual decrease in riparian vegetation after 1998.

3.3 Analysis of Landscape Phenology and Decadal Trends with MODIS Imagery

Figure 8 shows a map of the long-term trend in MODIS NDVI during the summer months (July, August, and September) for the entire Tarim basin, as well as an enlargement for the area between the Yuli and the Qiala Reservoir, around the Konqi and Tarim Rivers. Overall, there was an increase in summer NDVI across the agricultural areas—oases, Bingtuan (quasimilitary) farm areas, and smaller farms along rivers. As expected, there was no trend in NDVI in most desert areas. However, several areas showed unexpected decreasing trends in NDVI.

1. Areas outside the river channels that previously experienced flooding. The large brown patch in the center of Fig. 8 (bottom) is typical of this case. The area was flooded in 2000 to 2001 (Fig. 9), leading to a proliferation of green vegetation in subsequent years, but when the floodwaters did not return, the area experienced a gradual decline in NDVI.
2. Declining NDVI on slopes of the Tian Shan, particularly in the Kaidu watershed and the Bosten Lake basin. In these areas, there was a consistent gradual downward trend in NDVI, with the annual mean falling at a rate of ~0.08 to 0.09 per decade.

The detailed time-series of NDVI data for riparian zones on two reaches of the lower Tarim River are shown in Figs. 10(a) and 10(b), with summary data in Table 7. These are the lowest (below Argan) and second-lowest (Daxihaizi to Argan) reaches on the river, characterized by a relatively thin ribbon of riparian vegetation surrounded by desert, with little to no agriculture present. Both reaches showed the same general pattern, with both mean NDVI and amplitude of the seasonal cycle increasing from 2000 to 2008, then flattening or declining until 2012.

In contrast, Fig. 10(c) shows a very different temporal evolution for the area between the Konqi and the Tarim Rivers southeast of Yuli. The broad-scale floods of 2000 to 2001 (Fig. 9) produced large increases of NDVI and its seasonal amplitude during the immediately following years, but over the ensuing decade with no return of these floods, the landscape experienced a drying trend with reduced NDVI and less seasonal variation.

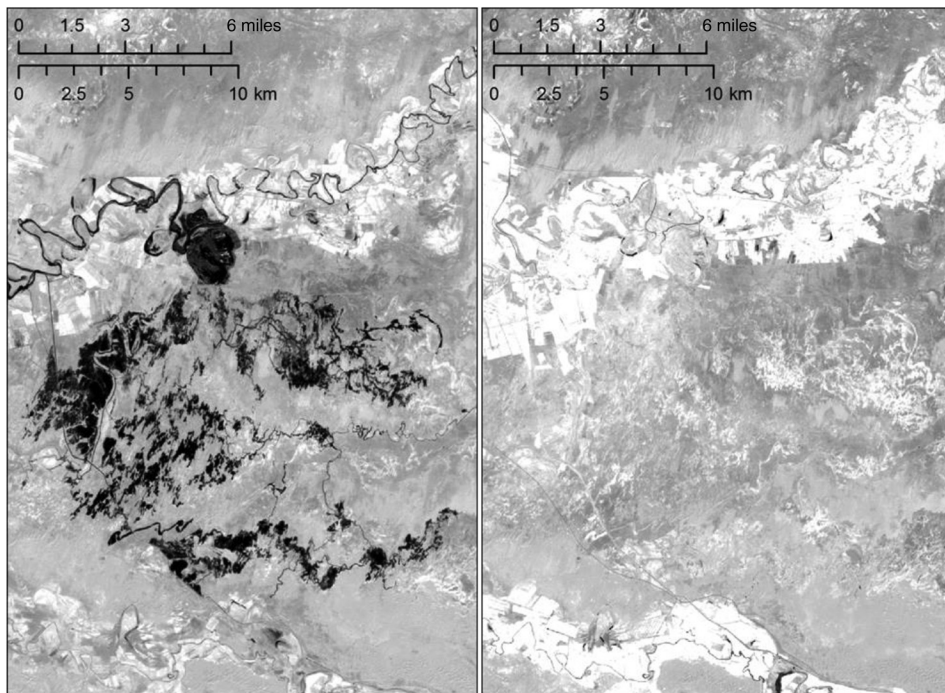


Fig. 9 Overbank flooding along the lower Konqi River, seen in Landsat band 4 images. (a) September 17, 2000, early in the flood episode. (b) August 7, 2011, no flooding.

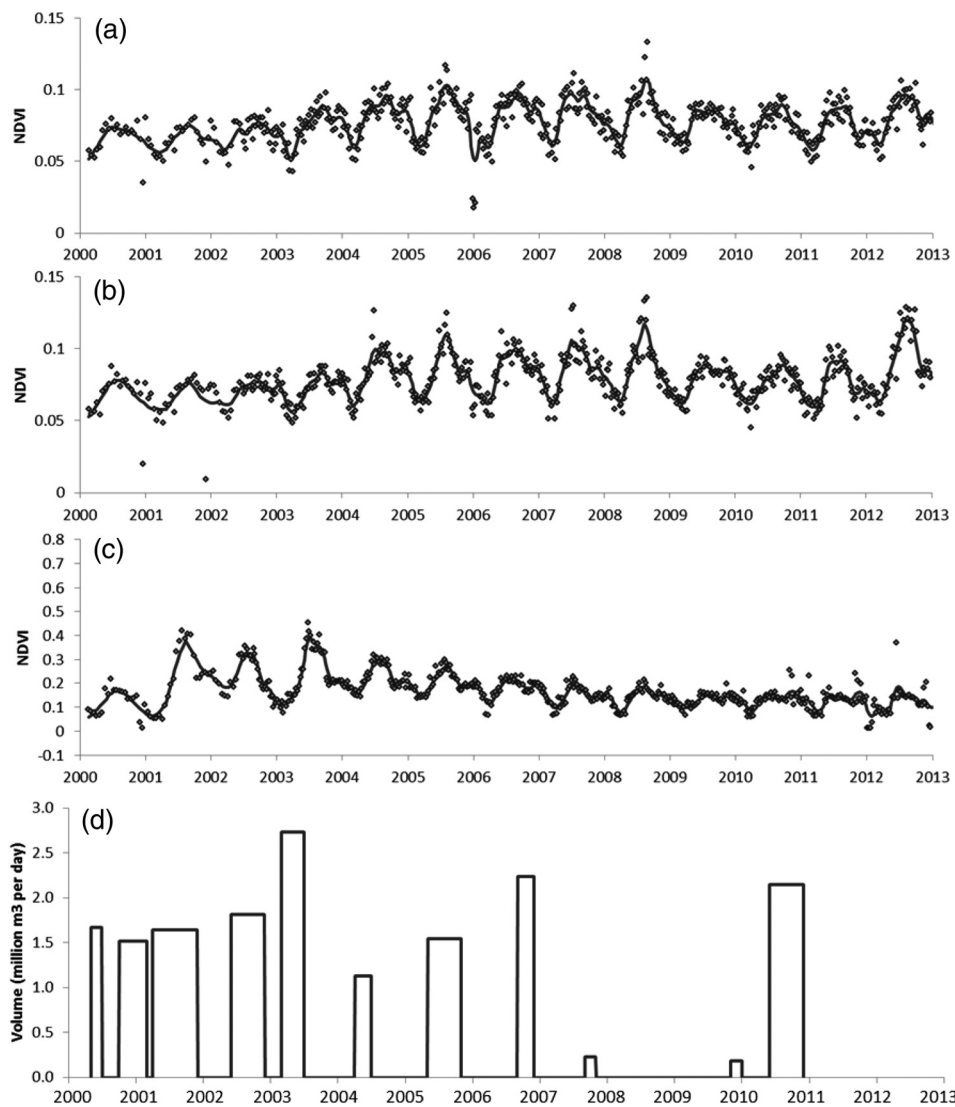


Fig. 10 MODIS NDVI time series of vegetation index data: (a) Tarim River below Argan; (b) Tarim River, Daxihaiizi to Argan; (c) area of overbank flooding in 2000 between Konqi and Tarim Rivers. Dots are raw MODIS NDVI, solid lines are LOESS smoothed versions with a 12-point timescale. For comparison to (a) and (b), panel (d) shows volume of water conveyances to the Lower Tarim River.

4 Discussion

The multiple analytical approaches used in this study provide complementary but not identical views of broad-scale changes in land use/land cover, and particularly in vegetation cover, from 1998 to 2012. Over this time period, irrigated agriculture (primarily cotton) expanded dramatically, nearly tripling its extent on the landscape. The obvious impact of this is to greatly increase the demand for water in the region. At the field level, cotton production in China requires $7180 \text{ m}^3 \text{ ha}^{-1}$ of water.²⁹ At that rate, the expansion of agriculture within our study area from 1998 to 2011 would have translated to a demand for an additional $1.7 \times 10^9 \text{ m}^3$ of water per year. However, that field-level water requirement is probably too low for South Xinjiang, where evaporation rates are higher than other cotton-producing regions of China. Assuming a requirement of $10,000 \text{ m}^3 \text{ ha}^{-1}$ (similar to those for other sites in Central Asia) suggests that annual demand for water within the study region has increased by $2.4 \times 10^9 \text{ m}^3$ of water. As land conversion for agriculture continues, this water demand will presumably increase as well.

Table 7 LOESS-filtered MODIS NDVI statistics for two reaches of the lower Tarim and one site of overbank flooding away from river channel. Annual mean and range (amplitude of seasonal cycle) are shown for each year.

Year	Tarim		Tarim		Overbank flood area	
	Below Argan		Daxihaizi to Argan		Between Konqi + Tarim	
	Mean	Range	Mean	Range	Mean	Range
2000	0.067	0.022	0.069	0.025	0.123	0.110
2001	0.065	0.019	0.065	0.018	0.214	0.316
2002	0.070	0.019	0.071	0.016	0.233	0.195
2003	0.074	0.037	0.072	0.028	0.235	0.280
2004	0.082	0.036	0.083	0.040	0.222	0.134
2005	0.082	0.048	0.084	0.045	0.204	0.124
2006	0.080	0.047	0.083	0.038	0.180	0.103
2007	0.083	0.037	0.085	0.045	0.151	0.104
2008	0.083	0.046	0.086	0.053	0.141	0.113
2009	0.077	0.022	0.078	0.026	0.131	0.055
2010	0.076	0.030	0.076	0.027	0.132	0.085
2011	0.074	0.030	0.075	0.032	0.129	0.088
2012	0.081	0.035	0.089	0.056	0.119	0.125

At the broad landscape scale, there has been little change in the total extent of unmanaged, natural vegetation (*Populus euphratitca* woodlands, shrublands, and grasslands) over the past decade. However, along the lower reaches of the Tarim River, downstream from Daxihaizi Reservoir, there was a gradual increase in the extent of riparian vegetation, particularly during the first half of the decade. After 2007, this increase stabilized or began to reverse itself. This pattern is evident in both the Landsat-derived estimates of fractional coverage of vegetation, as well as in the spatially coarser but temporally fine-scaled NDVI data from MODIS. As shown in Table 1 and Fig. 10(d), these trends qualitatively correspond to the timing of the intermittent conveyances of water into the lower Tarim, by transfer from the Konqi River and by the release of water from Daxihaizi reservoir—these conveyances were more extensive during the first half of the decade, then became smaller and more infrequent. The single large conveyance in late 2010 might have led to a resumption in the increase of greenness, but in the absence of further conveyances it is likely that any such increase will have been short lived.

There are indications that the lower Konqi River, downstream from the heavily irrigated Yuli oasis, may have experienced a decrease in riparian vegetation cover post-1998. It is suggestive that this occurs during the decade when water is being conveyed out of the Konqi River and into the Tarim, but establishing a causal relationship would require more detailed analysis [as shown in Figs. 5(c) and 5(d), there has been a rapid expansion of irrigated agriculture within the Konqi watershed itself, so transfers to the Tarim are not the only factor that could explain decreased water availability downstream].

More clearly, there are indications that intermittent, broad-scale flooding—including episodes in which floodwaters break out into new or former channels—are responsible for sudden increases in vegetation cover and greenness at the landscape scale, away from the immediate riparian zone that has been the focus of most ecohydrology studies on the Tarim River to date. Figures 8(b), 9, and 10(d) show this process and its aftermath. Considering the rhetorical importance of ecological restoration in the past decade's policy of water conveyances, it is worth considering what will happen at the broader landscape scale, not merely in the “green ribbon”

of riparian vegetation along the existing river channel itself. One plausible future scenario would involve more and more intensive management of flows within the channel, perhaps leading to modest groundwater recharge and riparian vegetation recovery along the river downstream from Daxihaizi Reservoir. At the same time, though, this more intensive management would lead to a decrease in the frequency and extent of stochastic, broad-scale flood episodes that in the past have intermittently conveyed large volumes of water to the landscape further away from the river channel. If sustained long enough, this change to the landscape-scale flood regime could have large consequences for the mosaic of vegetation communities in the region.

Each of the three analytical streams in this study contributes to a consistent picture of an evolving ecohydrological landscape, but the differences among the three suggest that they should be seen as complementary rather than redundant. The land cover classification and linear spectral mixture analysis methods were both applied to the same source data—multispectral imagery from Landsat-5 and -7. The land cover classification process, however, did not allow differentiation among riparian ecosystems with similar composition but different degrees of canopy cover. The spectral mixture analysis did provide that differentiation, but (in this study) did not distinguish between agricultural and natural vegetation. Using the two in combination provides a far more comprehensive view than either one alone. Meanwhile, the MODIS vegetation index data offer an unprecedented high temporal resolution, allowing the seasonal cycle to be resolved and interannual differences in its amplitude or other properties to be examined; but at the cost of a much coarser spatial resolution.

Over time, it is possible that platforms such as SENTINEL-2A/2B may support some of the temporally dense phenological analysis that now requires coarser-resolution systems such as MODIS, while simultaneously allowing finer-scale image classification and spectral mixture modeling. At the same time, however, there will be a push to use still higher-resolution systems (e.g., WorldView-3) for much more spatially detailed vegetation mapping. Thus, while individual sensors and constellations of similar sensors become more capable, the incentive for multi-sensor approaches will likely persist.

The methods used here should be readily adaptable to other arid landscapes, and indeed while the synergistic use of these different approaches is novel, variants of each individual method have been demonstrated elsewhere. The relatively lower frequency of cloud cover makes satellite remote sensing a particularly useful tool in arid regions. The existence of a long-term archive of historical imagery from Landsat (extending back to the 1980s at 30 m spatial resolution, and the 1970s at 79 m resolution) and MODIS (since 2000) provides a rich source for future studies of long-term change. Large-area and multitemporal studies benefit from freely available imagery, but ultrahigh resolution vegetation mapping may necessitate the purchase of more costly data from commercial satellite operators.

5 Conclusion

We have used three complementary approaches to examine the impacts of land cover change and water management on the Tarim and the Konqi river systems and their surrounding landscapes in Xinjiang, China. Spectral classification of a time series of Landsat images showed (as expected) that agriculture has expanded rapidly since the late 1990s, in part at the expense of natural riparian forest and shrub communities. The total area of natural, unmanaged riparian vegetation stayed approximately constant, but did so by dynamically expanding in some areas (e.g., along the lower Tarim) while experiencing losses elsewhere. Linear spectral mixture analysis added more detail to this picture, with the fractional cover of riparian vegetation changing little along the middle reaches of the Tarim River, whereas fractional cover increased following water conveyances on the Lower Tarim but decreased on the Konqi River. Finally, analysis of high temporal resolution image time series data from MODIS showed broad-scale patterns of increasing and decreasing greenness in different portions of the study area, including a landscape-scale response by vegetation to past episodes of overbank flooding.

Comparing the results from three different analytical approaches (land cover classification, spectral mixture analysis, and landscape phenology analysis) gives increased confidence in our findings about the nature and extent of environmental changes in the Tarim/Konqi region. In this case,

it shows that land use/land cover change and water management policy—both deliberate and inadvertent—are having large and spatially disparate impacts on the region's ecosystems. Over the coming decades, the forces driving change in the hydrology of the Tarim and Konqi basins—including land cover change, urbanization, industrialization, resource extraction, interbasin water transfers, channelization, decadal-scale climate variability, and long-term anthropogenic climate change—are expected to continue or in some cases intensify. Given the vast spatial scale of these river systems, remote sensing provides the only feasible way to monitor the effects of these changes on riparian and distal ecosystems. More broadly, the methods being used in this study should be considered for use in other arid regions with montane-sourced water systems under stress from growth, development, and climate change, from Central Asia to the Andes to the southwestern US.

Acknowledgments

This project was supported by the Rockefeller Center at Dartmouth College and the Porter Family Foundation. In Xinjiang, this work was also supported by the National Science and Technology Support Plan of China (No. 2014BAC15B02). Dartmouth undergraduate students Lusha Zhou, Abby Franklin, and Gerben Scherbier contributed to the analysis of the remote sensing data. We thank the anonymous reviewers for their valuable suggestions, which have improved the manuscript.

References

1. X. Hao et al., "Impacts of climate change and human activities on the surface runoff in the Tarim River basin over the last fifty years," *Water Res. Manag.* **22**, 1159–1171 (2008).
2. Y. Chen et al., "Response of riparian vegetation to water table changes in the lower reaches of Tarim River, Xinjiang Uygur, China," *Hydrogeol. J.* **16**, 1371–1379 (2008).
3. A. Sorg et al., "Climate change impacts on glaciers and runoff in Tien Shan (Central Asia)," *Nat. Clim. Change* **2**(10), 725–731 (2012).
4. T. Pieczonka et al., "Heterogeneous mass loss of glaciers in the Aksu-Tarim Catchment (central Tien Shan) revealed by 1976 KH-9 Hexagon and 2009 SPOT-5 stereo imagery," *Remote Sens. Environ.* **130**, 233–244 (2013).
5. Y. Chen et al., "Periodic changes of stream flow in the last 40 years in Tarim River Basin, Xinjiang, China," *Hydrol. Processes* **22**, 4214–4221 (2008).
6. J. Westermann, S. Zerbe, and D. Eckstein, "Age structure and growth of degraded *Populus euphratica* floodplain forests in north-west China and perspectives for their recovery," *J. Integr. Plant Biol.* **50**(5), 536–546 (2008).
7. Z. Ye et al., "Effect of the ecological water conveyance project on environment in the Lower Tarim River, Xinjiang, China," *Environ. Monitor. Assess.* **149**, 9–17 (2009).
8. T. Liu et al., "On the usefulness of remote sensing input data for spatially distributed hydrological modelling: case of the Tarim River basin in China," *Hydrol. Processes* **26**(3), 335–344 (2012).
9. L. Jiang et al., "Water resources, land exploration, and population dynamics in arid areas—the case of the Tarim River Basin in Xinjiang, China," *Popul. Environ.* **26**(6), 471–503 (2005).
10. Q. Zhou, B. Li, and A. Kurban, "Spatial pattern analysis of land cover change trajectories in Tarim Basin, northwest China," *Int. J. Remote Sens.* **29**(19), 5495–5509 (2008).
11. Z. Sun, N.-B. Chang, and C. Opp, "Using SPOT-VGT NDVI as a successive ecological indicator for understanding the environmental implications in the Tarim River Basin, China," *J. Appl. Remote Sens.* **4**, 043554 (2010).
12. Z. Sun et al., "Evaluation of ecological restoration through vegetation patterns in the lower Tarim River, China with MODIS NDVI data," *Ecolog. Inf.* **6**(2), 156–163 (2011).
13. J. Xu et al., "Climate change and its effects on runoff of Kaidu River, Xinjiang, China: a multiple time-scale analysis," *Chin. Geogr. Sci.* **18**, 331–339 (2008).
14. B. Li, Y. Chen, and X. Shi, "Why does the temperature rise faster in the arid region of northwest China?," *J. Geophys. Res.* **117**, D16115 (2012).
15. H. Wang et al., "Changes in daily climate extremes in the arid area of northwestern China," *Theor. Appl. Clim.* **112**(1–2), 15–28 (2013).

16. NCAR GIS Program, Climate Change Scenarios, version 2.0. Community Climate System Model, June 2004 version 3.0, <http://www.cesm.ucar.edu/models/ccsm3.0/> was used to derive data products. NCAR/UCAR. <http://www.gisclimatechange.org> (2012).
17. B. Li et al., "Temperature and precipitation changes in different environments in the arid region of northwest China," *Theor. Appl. Climatol.* **112**(3–4), 589–596 (2013).
18. J. Wu and D. Tang, "The influence of water conveyances on restoration of vegetation to the lower reaches of Tarim River," *Environ. Earth Sci.* **59**, 967–975 (2010).
19. US Geological Survey (USGS), "Earthexplorer," 2016, <http://earthexplorer.usgs.gov> (8 March 2016).
20. Exelis Visual Information Solutions, "ENVI Atmospheric Correction Module: User's Guide," Online at https://www.exelisvis.com/portals/0/pdfs/envi/Flaash_Module.pdf (2009).
21. R. Congalton and K. Green, *Assessing the Accuracy of Remotely Sensed Data: Principles and Practices*, 2nd Ed., CRC/Taylor & Francis, Boca Raton, Florida (2009).
22. ESRI, *World Imagery Web Map Service (WMS) Layer*, Esri, Redlands, California (2012).
23. R. Pontius and M. Millones, "Death to kappa," *Int. J. Remote Sens.* **32**(15), 4407–4429 (2011).
24. S. Stehman, "Estimating the kappa coefficient and its variance under stratified random sampling," *Photogramm. Eng. Remote Sens.* **62**, 401–407 (1996).
25. T. Lillesand, R. Kiefer, and J. Chipman, *Remote Sensing and Image Interpretation*, 7th Ed., John Wiley and Sons, New York (2015).
26. W. Cleveland and S. Devlin, "Locally weighted regression: an approach to regression analysis by local fitting," *J. Am. Stat. Assoc.* **83**, 596–610 (1988).
27. J. Peltier, "LOESS utility for excel" (2009), <http://peltiertech.com/loess-utility-for-excel/> (1 July 2016).
28. G. Snedecor and W. Cochran, *Statistical Methods*, 8th Ed., Iowa State University Press, Ames, Iowa (1989).
29. A. Chapagain et al., "The water footprint of cotton consumption: an assessment of the impact of worldwide consumption of cotton products on the water resources in the cotton producing countries," *Ecol. Econ.* **60**(1), 186–203 (2006).

Jonathan W. Chipman received his PhD from the University of Wisconsin-Madison in 2001. He is a geospatial scientist and director of the Citrin GIS/Applied Spatial Analysis Lab, Dartmouth College, New Hampshire, USA. In recent years, he has worked on a wide variety of remote sensing projects focusing on land cover, ecology, and freshwater systems. He is the coauthor of the textbook *Remote Sensing and Image Interpretation*, now in its 7th edition.

Xun Shi received his PhD from the University of Wisconsin-Madison in 2002. He is a professor of geography at Dartmouth College, New Hampshire, USA. He specializes in quantitative spatial analysis and modeling. He has done research and published extensively on spatial analytical methodologies and their applications, including public health, soil mapping, land use dynamics, and sustainable energy.

Francis J. Magilligan is a professor in the Geography Department at Dartmouth College and holds the Frank J. Reagan '09 Chair in Policy Studies. His research interests focus primarily on fluvial geomorphology and surface water hydrology with particular attention to stream channel and watershed responses to environmental change. In addition to his long-term interest in geomorphic responses to large floods, his recent research addresses the hydro-ecological impacts of dams and of dam removal.

Yaning Chen received his PhD from Northwestern University in 2000. He is a professor at the Xinjiang Institute of Ecology and Geography, Chinese Academy of Sciences, Xinjiang, China. He specializes in physical geography and has an extensive record of research and publications on ecological and hydrological processes.

Baofu Li received his PhD from the University of Chinese Academy of Sciences in 2013. He is an associate professor at Qufu Normal University, Shandong Province, China. He specializes in physical geography. He has done research and published extensively in climate change and water resources.